Room-temperature sputtered tungsten-doped indium oxide for improved current in silicon heterojunction solar cells

Han, Can; Zhao, Yifeng; Mazzarella, Luana; Santbergen, Rudi; Montes, Ana; Moya, Paul ; Yang, Guangtao ; Zhang, Xiaodan; Zeman, Miro; Isabella, Olindo

DOI
10.1016/j.solmat.2021.111082

Publication date
2021

Document Version
Final published version

Published in
Solar Energy Materials and Solar Cells

Solar Energy Materials & Solar Cells 227 (2021) 111082

Contents lists available at ScienceDirect

Solar Energy Materials and Solar Cells

journal homepage: http://www.elsevier.com/locate/solmat

Room-temperature sputtered tungsten-doped indium oxide for improved current in silicon heterojunction solar cells

Can Han [a,b,*], Yifeng Zhao [a], Luana Mazzarella [a], Rudi Santbergen [a], Ana Montes [a,c], Paul Procel [a], Guangtao Yang [a], Xiaodan Zhang [d], Miro Zeman [a], Olindo Isabella [a,**]

[a] Photovoltaic Materials and Devices Group, Delft University of Technology, Delft, 2628 CD, the Netherlands
[b] Shenzhen Institute of Wide-bandgap Semiconductors, Shenzhen, 518055, China
[c] Faculty of Sciences of University of Lisbon, Lisbon, 1749-06, Portugal
[d] Institute of Photoelectronic Thin Film Devices and Technology of Nankai University, Tianjin, 300350, China

ARTICLE INFO

Keywords:
Tungsten-doped indium oxide
Silicon heterojunction solar cell
Improved near-infrared response
Room temperature transparent electrode

ABSTRACT

The window layers limit the performance of silicon heterojunction (SHJ) solar cells with front and back contacts. Here, we optimized tungsten-doped indium oxide (IWO) film deposited by radio frequency magnetron sputtering at room temperature. The opto-electrical properties of the IWO were manipulated when deposited on top of thin-film silicon layers. The optimal IWO on glass shows carrier density and mobility of 2.1×10^{20} cm^{-3} and 34 $cm^2 V^{-1}s^{-1}$, respectively, which were tuned to 2.0×10^{20} cm^{-3} and 47 $cm^2 V^{-1}s^{-1}$, as well as 1.9×10^{20} cm^{-3} and 42 $cm^2 V^{-1}s^{-1}$, after treated on *i/n*/glass and *i/p*/glass substrates, respectively. Using the more realistic TCO data that were obtained on thin-film silicon stacks, optical simulation indicates a promising visible-to-near-infrared optical response in IWO-based SHJ device structure, which was demonstrated in fabricated devices. Additionally, by adding an additional magnesium fluoride layer on device, the champion IWO-based SHJ device showed an active area cell efficiency of 22.92%, which is an absolute 0.98% efficiency gain compared to the ITO counterpart, mainly due to its current gain of 1.48 mA/cm^2.

1. Introduction

For silicon heterojunction (SHJ) solar cells, increasing short-circuit current density (J_{SC}) or fill factor (*FF*) is an attractive route to further improve device efficiency, since minority carrier effective lifetimes at one-sun injection levels approach the Auger and radiative recombination limit of the commonly-used silicon wafer base [1]. This contribution mainly focuses on J_{SC}. In SHJ with front and back contacts, a front transparent conductive oxide (TCO) on top of thin-film silicon layers is required to ensure sufficient lateral carrier transport towards metal contacts. Further, it acts as an anti-reflection coating on the illuminated side of the solar cell [2]. On the other hand, to serve as a contacting and optical reflector, rear TCO is also required for practical SHJ device application [3,4]. To date, the development of TCOs with high mobility and low free carrier parasitic absorption (FCA) has facilitated promising J_{SC} of over 40 mA/cm^2 [5,6].

Indium oxide (In_2O_3) has been proven to be an excellent host material for developing high performance TCOs with variable dopant introduction [7,8]. By far, the choice of dopants that induce high mobility in TCOs has largely been empirical, in which In_2O_3 doped with transition metal elements (such as Zr [5,9], Ti [10], Mo [11], Ce [12], Hf [13], W [8,14–16]) represent an attractive group. As suggested by Zhang *et al.* [17], the high mobility potential of the transition metal doped In_2O_3 could be explained by the high Lewis acid strength, which can be calculated from $L = Z/r^2 - 7.7\chi_z + 8.0$, where r is the ionic radius related to the electrostatic force due to the oxidation state Z of the ion and χ_z is the electronegativity of the element in the respective oxidation state. W^{6+} exhibits a high L of 3.158 due to its low ionic radius and high oxidation state. The W dopant with higher L compared to In^{3+} (1.026) in the host compound attracts electronic charge from the O^{2-} 2*p* valence band, resulting in the screening of the dopant's effective charge (Z). This screening effect weakens the interaction between the carriers and dopant ions, which means that the dopant's activity as a scattering center is receded thus high mobility is achievable. In addition, the ion radii of W^{6+} and In^{3+} are 0.6 Å and 0.8 Å, respectively, the tungsten dopant can substitute indium site in the lattice of In_2O_3, high

* Corresponding author. Photovoltaic Materials and Devices Group, Delft University of Technology, Delft, 2628 CD, the Netherlands.
** Corresponding author.
E-mail address: C.Han-1@tudelft.nl (C. Han).

https://doi.org/10.1016/j.solmat.2021.111082
Received 1 February 2021; Received in revised form 15 March 2021; Accepted 24 March 2021
Available online 14 April 2021

crystallinity of IWO in In_2O_3 polycrystalline structure has been reported [18]. Moreover, W^{6+} substituting for In^{3+} can still provide an electron even when associated with interstitial oxygen impurities (O^{2-}) in the lattice by forming charged complexes, $[(W_{In}{}^{\cdots})\, O_i'']^{\bullet}$, as oppose to Sn^{4+} dopants in ITO, which become deactivated by forming neutral complexes, $[(2Sn_{In}^{\bullet})O_i'']$. This means that for the same number of carrier concentration, there may exist much less of dopant scattering centers in IWO film than in the commonly used ITO film [19]. All the above factors contribute to a high carrier mobility potential in IWO film [7]. Furthermore, tungsten doped indium oxide (IWO) shows complementary features in combining the advantages of indium oxide and tungsten oxide; thus it provides possibilities in manipulation of different contact characters [20]. As a consequence, IWO is a promising candidate for transparent electrode in photovoltaic devices [16].

For the fabrication of IWO layers, a wide range of deposition techniques have been utilized, such as pulsed laser deposition (PLD), reactive plasma deposition (RPD, or arc plasma ion plating, or high-density plasma-enhanced evaporation), magnetron sputtering [7,12,14]. In order to obtain decent carrier mobility above 60 $cm^2\ V^{-1}\ s^{-1}$, a deposition temperature of above 300 °C was utilized for quite a long time [7]. This is not suitable for SHJ devices, which require a process temperature below 250 °C, or even lower [4,21]. Since 2013, Liu *et al.* have been working on developing SHJ-targeted IWO film via RPD approach [15,16,19,22]. Similar technique was also utilized by Koida *et al.* [8,23]. Besides, Lerat *et al.* applied radio frequency (RF) magnetron sputtered hydrogenated IWO for SHJ application [24]. The above-mentioned techniques were using a deposition or post-deposition annealing treatment above 150 °C.

Accordingly, it is imperative to study the opto-electrical properties and the application of a low thermal budget IWO layer. Herein, we present an IWO optimization at room temperature (RT) by RF magnetron sputtering. The opto-electrical properties of the optimized IWO film are evaluated on top of thin-film silicon layers. Finally, the performances of IWO-based SHJ solar cells are tested and compared to reference devices with ITO.

2. Methodology

Deposition of TCO films: TCO films were deposited on corning glass substrates by RF magnetron sputtering technique (Polyteknic AS). Prior to sputtering, the substrates were cleaned in acetone and isopropyl alcohol sonication baths for 10 min, respectively. IWO films were deposited from a ceramic target which is made of 95 wt% In_2O_3 and 5 wt % WO_3. Argon and 1% oxygen in argon were utilized as the process gas. The chamber was evacuated to a base pressure below 1×10^{-7} mbar before deposition to eliminate the contribution of the water during the processing. All depositions were performed at room temperature without any intentional heating, with the chamber pressure of 4.0×10^{-3} mbar, (Ar + O_2) flow of 20 sccm, and power density of ~0.8 W/cm^2. The deposition rate of the optimized IWO films was ~2 nm/min. ITO reference films were grown from a ceramic target consisting of 90 wt% In_2O_3 and 10 wt% SnO_2. The ITO depositions were done at substrate temperature of 110 °C, chamber pressure of 2.0×10^{-2} mbar, Ar flow of 50 sccm (0.05% O_2), and power density of ~1.8 W/cm^2. The deposition rate of ITO layer was ~6 nm/min.

Fabrication of SHJ solar cells: First, 4-inch float zone (FZ) 280-μm thick n-type flat (100) oriented wafers (1–5 Ω cm) were randomly textured in a heated solution composed of 5% TMAH and 2.4% ALKATEX 8 from GP-Solar-GmbH. The double-side textured wafers were subsequently cleaned in two subsequent baths of HNO_3 for 10 min a HNO_3 99% bath (RT, 10 min) and HNO_3 69.5% (110 °C, 10 min) for removing the organic and inorganic contaminations, respectively. Wafers were dipped in 0.55% HF for 4 min to remove the superficial oxide layer and immediately after loaded into the plasma enhanced chemical vapour deposition (PECVD) system. Then, SHJ cell precursors with front 10-nm thick *i/n* stack and rear 26-nm thick *i/p* stack thin-film silicon layers were prepared. Nominal 75-nm and 150-nm thick TCO films were sputtered on the front and rear sides of the wafers, respectively, through hard mask, which defines different cell areas on each wafer. The TCO layers of the front and rear side were deposited with the same parameters. A geometrical factor of 1.7 was used in the thin film silicon layer growth and TCO sputtering on textured wafer surface, with respect to that on flat wafer. After sputtering, the IWO-based cell precursors were annealed in air at 180 °C for 5 min for curing purposes. We note that ITO-based devices maintained good passivation qualities after ITO sputtering; thus no subsequent post annealing treatment was applied on corresponding cell precursors. Front metal contacts were RT electroplated Cu fingers, with an underlying 100-nm thick Ag as seed layer [25]. The photolithography process with organic photoresist (AZ ECI3027 from Microchemicals) was used to define the contact area for metallization. The rear metal contact was 500-nm thick thermally evaporated Ag. For a double layer anti-reflection coating purpose, 90-nm thick MgF_2 layer was e-beam evaporated on the front side of the completed SHJ devices.

Characterizations: The opto-electrical properties of the TCO films were evaluated with a Hall effect measurement setup HMS-5000 (ECOPIA CORP) and with a spectroscopic ellipsometry (SE) system M-2000DI system (J.A. Woollam Co., Inc.). The former gave information on the carrier density (N_e), carrier mobility (μ_{hall}), and resistivity (ρ) of the TCO films. The latter was instead used to derive the film thickness (d), wavelength-dependent complex refractive index (n, k), and absorption coefficient (α) spectra. The optical band gap (E_g) was extracted from Tauc plot [26]. The single and multi-layer strategy approach in SE modelling is described in Fig. S1. Besides, the transmittance and reflectance spectra were obtained from a PerkinElmer Lambda 1050 system. Additionally, the crystalline structure of the films was studied with the X-ray diffraction (XRD) technique. The XRD spectra were obtained on an XPERT-PRO diffractometer system with spinning stage (Spinner PW3064), and a Cu Kα radiation from the X-ray tube with normal focus was used (Cu Kα = 1.5406 Å). Morphological images of the TCO layers were detected from field-emission scanning electron microscope (FE-SEM) via Hitachi Regulus 8230, and surface roughness of the thin-film silicon layers was obtained from atomic force microscope (AFM) measurement setup and NOVA program.

Simulation: Ray-tracing GenPro4 optical simulations [27] of our SHJ device structure were performed based on double-side textured c-Si wafer with SE-fitted complex refractive index of each functional layer as input.

Solar cell measurements: Quasi-steady-state photoconductance (QSSPC) lifetime measurements were performed using a Sinton Instruments WCT-120 on cell precursors before and after the TCO sputtering. Current-voltage (I–V) characteristics of complete SHJ devices were measured using a class AAA Wacom WXS-156S solar simulator under 1-sun illumination conditions (100 mW cm^{-2}, AM 1.5G). The error bar in reported figures was calculated by dividing the standard deviation by the square root of number of measurements. External quantum efficiency (EQE) measurements were performed to evaluate wavelength-dependent optical response and to extract the short-circuit current density J_{SC_EQE}. The active area power conversion efficiency of the devices was calculated from the product of V_{OC}, FF, and J_{SC_EQE}. The reflectance of solar cells was also measured via the PerkinElmer Lambda 1050 system.

3. Results and discussion

3.1. Opto-electrical properties optimization and material analysis of 75-nm thick IWO films on glass substrate

Hall measurements show that the IWO films are *n*-type semiconductor. Fig. 1(a) shows their carrier density (N_e), mobility (μ_e), and resistivity (ρ) change as function of O_2-to-Ar flow ratio (X). For X increasing from 0 to 0.50%, N_e monotonously decreases, while μ_e first

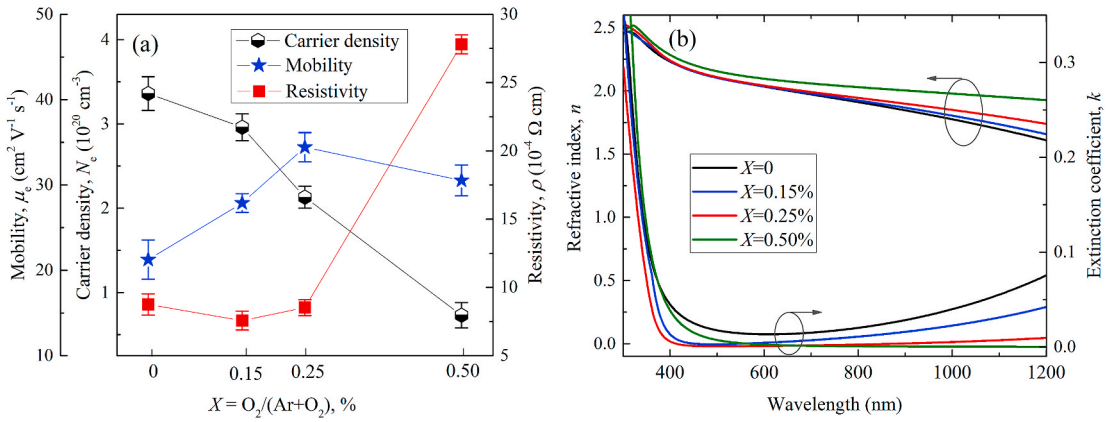

Fig. 1. (a) N_e, μ_e, and ρ of the as-grown IWO films with a variable O_2-to-Ar flow ratio (X), based on six groups of experimental data. (b) Complex refractive index of the IWO films for different X.

rises and then goes slightly down. Consequently, the ρ value first decreases and then rises up. The highest μ_e of 34 cm^2 V^{-1}s^{-1} was obtained at X = 0.25%. This is higher than the reported <20 cm^2 V^{-1}s^{-1} of RT-sputtered IWO layer at room temperature [28]. However, we note that both N_e and μ_e of our as-deposited layer are lower than that of reported RT grown IWO films from RPD approach [14,19]. Possibly, as compared to the sputtering process, the high-density plasma density in RPD technique provides higher reactivity of the evaporated species from the tablet material, which promotes higher effective doping of W dopant and thus produces excess electrons and higher N_e in the IWO film [14,29,30]. The charge screening effect of more effective W dopant and the plausibly increased densification/crystallization of the film, contribute to a higher μ_e in the IWO film [7,14,19].

Furthermore, the electrical properties of the TCOs correlate their optical properties. Fig. 1(b) displays the complex refractive index of the IWO films. The IWO deposited at X = 0.25% yields the largest optical bandgap (E_g) in UV range and low absorption in NIR range, while the IWO deposited at X = 0.50% shows an E_g shrinkage (Moss-Burstein effect [31]) and rather high ρ due to its lowest N_e. Thus, it was not considered for use in devices.

Fig. 2(a–b) present the XRD patterns corresponding to an In_2O_3 cubic bixbyite crystal structure and SEM images of the IWO layers grown with different X. One can see from both figures that, with increasing X from 0 to 0.50%, the crystallization of the as-deposited IWO films largely improves. This is possibly due to the increased stoichiometric composition of the film [32]. For the XRD results with X = 0 and X = 0.15%, the absence of diffraction peaks is indicative of mostly amorphous films. Further, from corresponding SEM images, we additionally observe the characteristic crystalline grain evolution, indicating a limited sensitivity of the XRD measurement in detecting low crystalline materials [9]. From Fig. 2(b), the grain size of the IWO films shows a decreasing trend with increased X, indicating more grain boundaries (GBs) that act as carrier scattering defects. Therefore, combined with the data shown in Fig. 1, the monotonously decreased N_e from X = 0 to X = 0.50% is mainly caused by a continuously increased oxygen incorporation, which occupies oxygen vacancies (V_O) that provide additional electrons in the IWO films [33]. Whereas the μ_e could be influenced by the compensation of decreased point defect scattering from V_O elimination, and GB scattering as mentioned above in Fig. 2 (b) [7]. In addition, the carrier transport at GBs is also influenced by the N_e change [34–36]. As a consequence, μ_e firstly rises from X = 0% to X = 0.25%, then drops with a further increased X to 0.50%.

Fig. 3 compares the absorption coefficient spectra of the optimal IWO grown from X = 0.25% to the ITO reference, with the inset table showing the parameters of N_e, μ_e, ρ and E_g. Notably, in the short wavelength range, the IWO with lower N_e shows a larger optical bandgap (E_g) than ITO, which is opposite to the well-known Moss-Burstein effect [31]. Presumably, it indicates a smaller effective electron mass in the IWO film structure [7,11]. Besides, with respect to ITO film, the lower absorption coefficient (α) of IWO layer in the NIR region could be explained by the classical Drude theory [37,38]. In addition, to further confirm the observations, we compared the absorptance curves of IWO

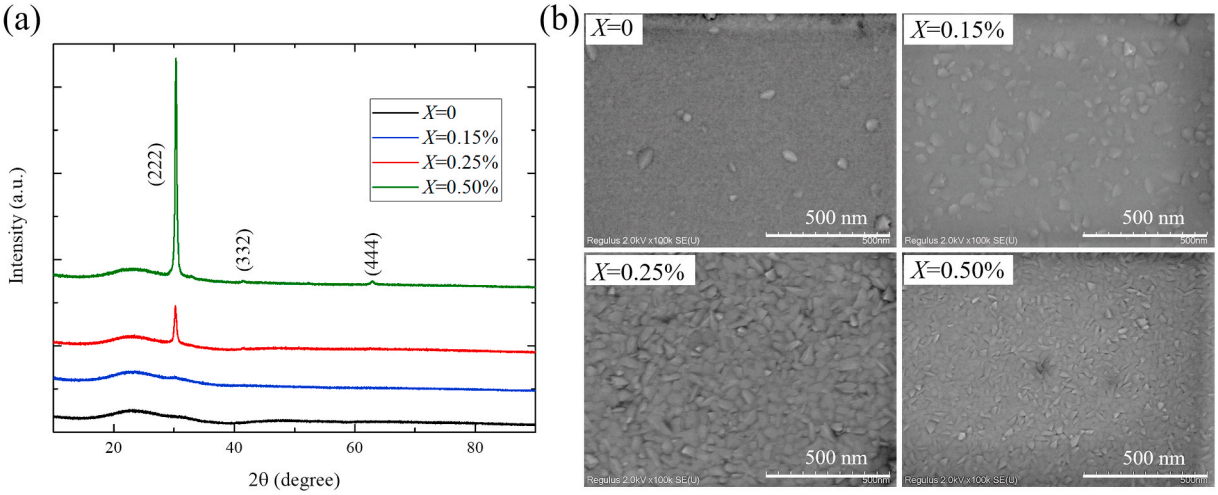

Fig. 2. (a) X-ray diffraction patterns, and (b) scanning electron microscope images of IWO films deposited with different O_2-to-Ar flow ratios (X).

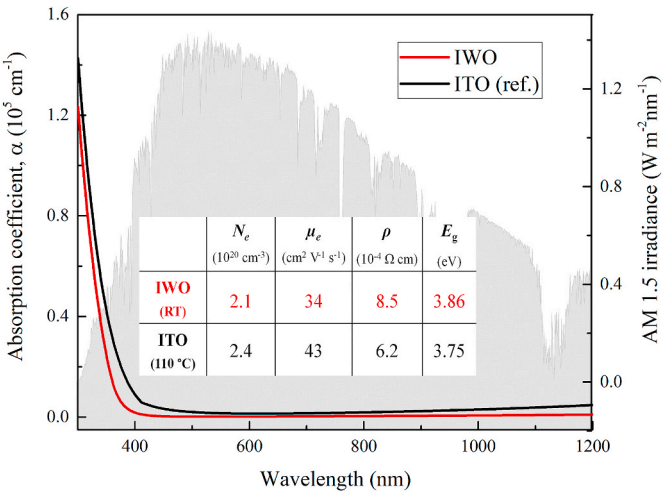

	N_e (10^{20} cm^{-3})	μ_e (cm^2 V^{-1} s^{-1})	ρ (10^{-4} Ω cm)	E_g (eV)
IWO (RT)	2.1	34	8.5	3.86
ITO (110 °C)	2.4	43	6.2	3.75

Fig. 3. SE-fitted absorption curves and inset table with opto-electrical properties of the optimized IWO and ITO reference films deposited at RT and 110 °C, respectively.

and ITO films which were calculated from 1-*R*-*T*, as shown in Fig. S2, which shows the same trend as we observed from Fig. 3.

3.2. IWO on top of thin film Si layers and optical Genpro4 simulation

Fig. 4(a–d) show the N_e and μ_e values of nominal 75-nm thick TCOs on glass and on *i*/*n*/glass and *i*/*p*/glass, respectively. Our lab-standard ITO film acts as a reference, and the *i*/*n* and *i*/*p* thin-film silicon layer stacks are in the same layer thickness as used in SHJ devices. We note that a hot-plate annealing at 180 °C for 5 min was performed on the RT-deposited IWO samples. This is a required step to recover the sputter damage of the passivation quality of the SHJ cell precursors (see Fig. S3), which could also potentially improve the electrical property of the IWO/*p*-layer interface [39]. For the IWO layers, deposition on either glass or thin-film silicon does not influence μ_e, whilst it mildly adjusts N_e. After annealing, the IWO films show a slightly lower N_e from 2.1 × 10^{20} cm^{-3} on glass substrate to 2.0 × 10^{20} cm^{-3} on *i*/*n*/glass and 1.9 × 10^{20} cm^{-3} on *i*/*p*/glass substrates, respectively. The N_e decreases reflect oxygen incorporation during the annealing process. On the other hand, upon annealing, the μ_e increases from 34 cm^2 V^{-1}s^{-1} on glass substrate to 47 cm^2 V^{-1}s^{-1} on *i*/*n*/glass and 42 cm^2 V^{-1}s^{-1} on *i*/*p*/glass substrates, respectively. This phenomenon could be associated with an increased Lewis acid strength (*L*) as introduced in Introduction part. After annealing treatment, tungsten dopant with a higher *L* could be reached due to a higher oxidation state of tungsten ions, which leads to an increased carrier mobility [7,32,40,41]. Additionally, with respect to as-deposited states, the μ_e increases in annealed IWO layers on *i*/*n*/glass and *i*/*p*/glass substrates are different, indicating that the μ_e is also influenced by (i) increased crystallization, as implied by the XRD patterns and SEM images in Fig. S4, and (ii) possible defect passivation of thermally effused hydrogen from underlying thin-film silicon layers [42,43]. Furthermore, with respect to glass substrate, the as-deposited ITO film on *i*/*n* stack shows constant μ_e and mildly increased N_e, while the ITO layer on *i*/*p* stack displays distinct μ_e drop together with N_e rise. The N_e change could be partially owing to the diffused hydrogen from the thin film underneath, which has been elucidated by Cruz *et al.* [42], Ritzau *et al.* [43] and Huang *et al.* [39]. Regarding the observed μ_e drop for the ITO on *i*/*p* stack, we exclude the cause from the substrate surficial roughness as observed by Cruz et al. [42]. In fact, AFM measurements show quite similar root-mean-square roughness values of 1.11 nm and 1.23 nm for our *i*/*n* and *i*/*p* stacks, respectively. Plausibly, our N_e and μ_e change is also correlated with additional features, such as crystallizations of both TCOs and thin-film Si layers and their inherent interactions, hydrogen effusion behaviour in dependence of temperature/ambience, TCO/Si interfacial oxide influence on carrier transport. Elaborated study still needs to be carried out to fully understand the interaction between IWO and doped thin-film layers. Additionally, it is worth pointing out that the substrate topology such as textured wafer surface might also have an impact on the TCO properties [44,45], which remains to be investigated via appropriate

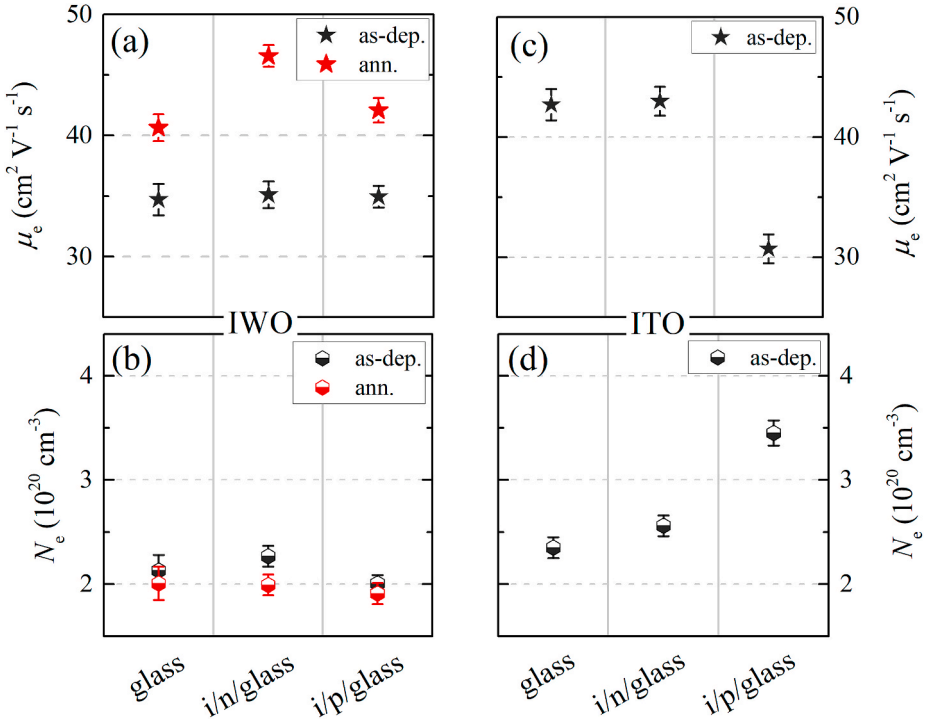

Fig. 4. (a) μ_e and (b) N_e of the as-deposited and annealed IWO films on different substrates; (c) μ_e and (d) N_e of as-deposited ITO layers on different substrates. The results are based on three groups of experimental data.

characterization approaches.

Fig. 5 shows the corresponding absorption coefficient (α) curves versus wavelength of TCOs on different substrates. Basically, all the IWO layers show favourable lower α than reference ITO films along the vis-NIR range. Regarding the IWO layers on thin-film silicon layers, with respect to the IWO films on *i*/*n*/glass and *i*/*p*/glass substrates, the different α transition in the UV range is possibly related to the thermally-effused hydrogen from underlying thin-film silicon layers, since both interstitial and substitutional hydrogen have been proven to act as shallow donors in In_2O_3 system [42,43,46]. Additionally, the α changes of the TCOs in the NIR region could be aligned with the classic Drude theory [37,38]. Overall, we may conclude that with thin-film silicon layer underneath, the top TCO film could be manipulated both electrically and optically, which needs to be considered in device simulations as well as in practical cell fabrication.

Fig. 6(a–c) show GenPro4 optical simulation results of comparative SHJ devices based on IWO and ITO counterpart. Fig. 6(a–b) are the simulated absorptance curves of IWO- and ITO-based SHJ structure, in which the TCO data obtained from thin-film silicon stacks were used. The results based on TCO data obtained on glass substrates were provided in Fig. S5(a-b). From Fig. 6(a–b), the implied photocurrent density in c-Si absorber was calculated to be 40.3 mA/cm^2 in IWO cell and 38.5 mA/cm^2 in ITO cell. As compared to ITO cell, the outstanding optical advantage of IWO cell is ascribed to the much less parasitic absorption in IWO layer. Fig. 6(c) displays the optical losses corresponding to reflection, parasitic absorption from thin-film silicon, TCO, and rear metal components. In Fig. 6(c), the results from simulations based on TCO data obtained on glass substrates are also included. With respect to the results from data on glass substrates, the IWO cell shows a lower parasitic absorption in TCO layer, while ITO cell shows an increased parasitic absorption in TCO layer. This is related to their different changing trends in N_e, as shown in Fig. 4 [37]. In addition, we notice that the total refection loss in IWO cell is visibly higher than in ITO cell. Following the approach as utilized in Ref. [47], we decomposed the total reflectance into front side reflectance (R_1) and rear side internal reflectance (R_2), which are indicated in Fig. 6(d). The R_1 and R_2 are 1.3 mA/cm^2 and 1.6 mA/cm^2 for IWO cell, and 1.5 mA/cm^2 and 0.5 mA/cm^2 for ITO cell, respectively. This means that the high reflection loss in IWO cell comes from its high R_2 value, indicating that large amount of NIR light escapes after passing through the cell. While in ITO cell such NIR light is mainly absorbed in the TCO, this is not displayed in the reflection loss. In this regard, the higher R_2 in IWO cell may not be optically detrimental since there is still possibility to make use of it with appropriate manipulation strategy. To summarize, the interactive opto-electrical properties of TCO with underlying layers need to be considered in device design, and our IWO layer indicates a promising optical outperformance in SHJ cell over ITO counterpart.

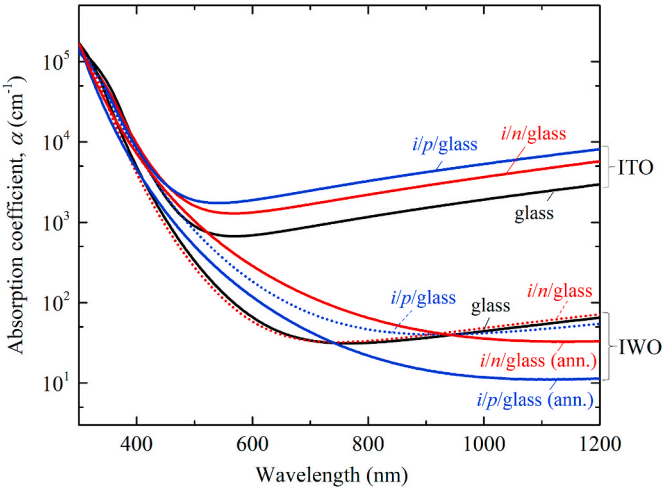

Fig. 5. SE-fitted absorption coefficient (α) curves of TCOs on top of different substrates.

3.3. Devices performance

Fig. 7(a–d) depict the measured IWO- and ITO-based SHJ cell parameters. The metallization approach is room temperature Cu-plating. For each batch, we tested variable devices in different metal design, all the devices in the same design showed similar comparative trend, and only the optimal 8.97 cm^2-cell results are summarized in Fig. 7. The implied-V_{OC} of the SHJ cell precursors varied from 720 to 735 mV (not shown here). From Fig. 7(a), the average V_{OC}, especially for IWO cells, is approaching 730 mV, due to the RT-Cu-plating metallization [25]. As for the optical response in Fig. 7(b), all the IWO cells showed notably higher J_{SC} than ITO devices, which agrees with the previous optical simulation results as shown in Fig. 6. We notice that the J_{SC} improvement from reference ITO cell to IWO cell was generally 0.8–1.4 mA/cm^2, which is smaller than the 1.8 mA/cm^2 as predicted from Genpro4 simulation. This may be ascribed to the electrical carrier transport/collection difference in the two kinds of devices, or possible underestimation on the simulated parasitic absorption of IWO layers, since reflection-type spectroscopic ellipsometry has been reported to present limited sensitivity for weak light absorption [48,49]. Additionally, from Fig. 7(c), the IWO cells showed slightly higher *FF* and lower series resistance ($R_{s,SunsVoc}$) than the ITO-based counterpart. This possibly originates from a favourable band alignment at the IWO/doped Si layer interfaces, as the IWO exhibit different work-function than ITO [20,50]. The IWO cells outperformed ITO devices due to their advantage in both optical and electrical aspects, as displayed in Fig. 7(d). With respect to ITO-SHJ cells, the averaged cell efficiencies of IWO-SHJ cells show absolute improvements of 0.98%. Our comparative cell results are in agreement with the observations from Ding *et al.* [6]. It is noteworthy that Ding *et al.* used hydrogenated IWO layers, which presented both higher μ_e and N_e as compared to our IWO film. According to Ding *et al.* [6], as compared to ITO cell, their J_{SC} increase is less, and *FF* increase is higher in IWO cell than in our case. Plausibly, the phenomena are related to the hydrogen inclusion in their IWO layer, which generates more dopants to ensure a good conductivity, yet results in a probability to compensate its optical property [51,52]. Additionally, we note that the measured J_{SC} in our *I*–*V* measurements was a bit higher than the integrated J_{SC_EQE} from EQE curve, similar phenomenon is also seen in Ref. [53]. Below we report the active area power conversion efficiency to avoid such a measurement error from the different light sources and metal fractions in the illumination area.

To minimize the above-mentioned high reflection loss in IWO cell (Fig. 6), we further introduced the so-called double layer anti-reflection coatings (DLARC). By adding an additional non-absorptive layer with appropriate thickness and refractive index of ~1.5 @ 600 nm, we can further decrease the reflection losses on device level [5,16,54,55]. Fig. 8 and Table 1 show the EQE, 1-*R* and cell parameters of our optimized IWO-based SHJ device and its ITO counterpart, with and without (w/o) a 90-nm thick MgF_2 top layer. The MgF_2 optical parameters and the simulative optimization with MgF_2 thickness on our IWO cell structure are shown in Fig. S6(a-b). From Fig. 8, compared to the devices without MgF_2 on top, the cell with MgF_2 layer showed significantly improved optical responses. Especially the J_{SC_EQE} of the IWO cell was improved from 39.41 mA/cm^2 to 40.16 mA/cm^2. This is mainly caused by a boosted performance in the short wavelength range (300–550 nm), resulting from the decreased reflectance of the cell surface, as we can clearly see from the 1-*R* curve. Finally, with adding a MgF_2 layer on top of the IWO device, the active area power conversion efficiency was improved from 22.52 to 22.92%.

Now we look at the EQE curves of the IWO cell and ITO cell in Fig. 8. Before applying the MgF_2 top layer, the IWO cell displays lower blue response in 300–600 nm (−0.46 mA/cm^2) and significantly higher

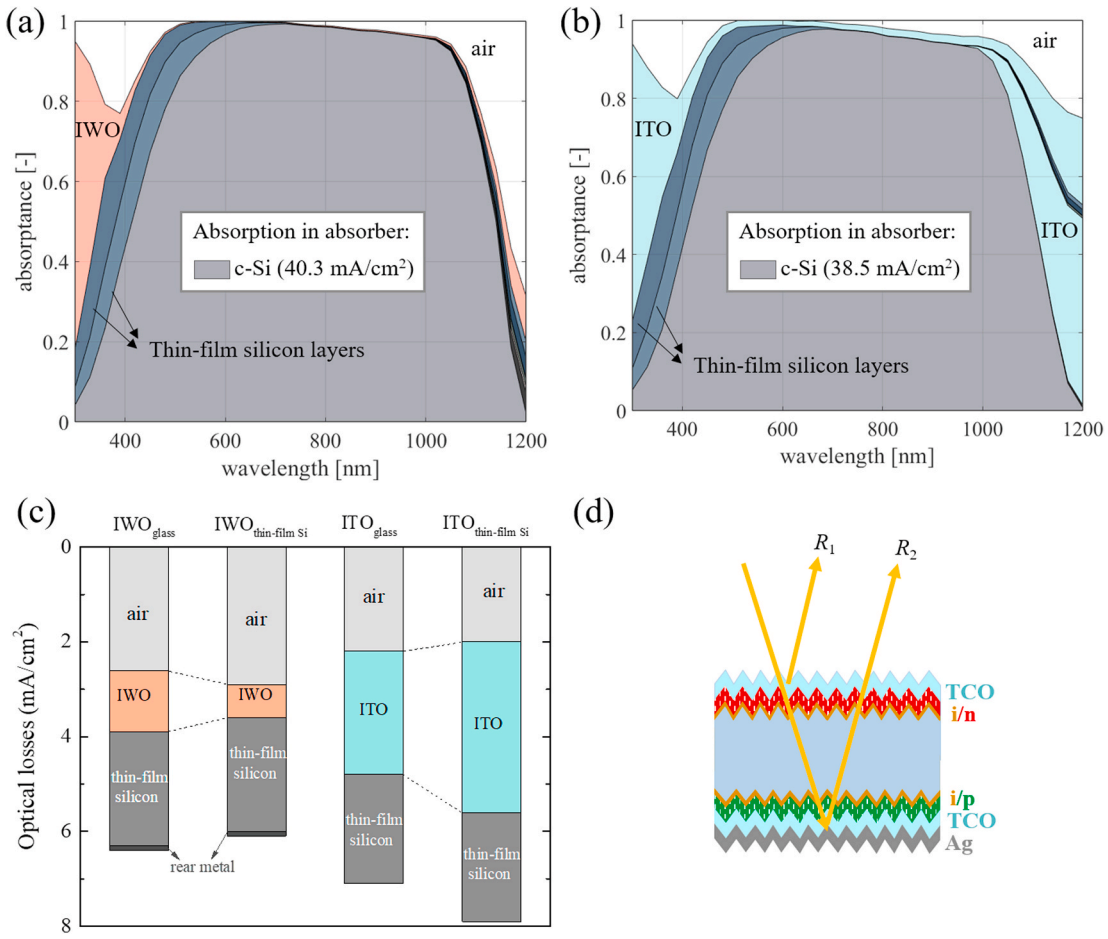

Fig. 6. Optical simulations performed by GenPro4 software of (a) IWO- and (b) ITO-based SHJ solar cells, in which the TCO data gathered from thin-film silicon layers were taken into consideration. (c) Overview of optical losses from different components. The simulations are performed using the TCO n,k data set obtained as indicated on the *x*-axis. (d) Sketch of individual reflection losses corresponding to the front and rear sides of our SHJ cell structure. (For interpretation of the references to colour in this figure legend, the reader is referred to the Web version of this article.)

response in vis-NIR region in 600–1200 nm (+1.74 mA/cm^2), as compared to ITO cell. After adding the top MgF_2 layer, the IWO/MgF_2 cell outperformed ITO/MgF_2 cell in the whole wavelength range, which corresponds to a 0.44 mA/cm^2 gain in the 300–600 nm region and a 1.04 mA/cm^2 gain in 600–1200 nm region, respectively. According to Fig. 3, the IWO layer has a higher E_g value of 3.86 eV than the 3.75 eV of ITO layer, while the IWO cell shows a lower blue response, as compared to ITO cell. To elaborate that, we performed optical band gap (E_g) plots of the TCOs on top of thin-film silicon stacks at the illuminated side of our SHJ device, as shown in Fig. S7. The extracted E_g values are 3.81 eV and 3.87 eV for IWO and ITO layers, respectively. Combined with Fig. 4, this more realistic comparison is in accordance with the Moss-Burstein effect [31] and well explains why the IWO cell shows a lower blue response than ITO cell. Additionally, this difference is not existing after applying MgF_2, and the J_{SC_EQE} improvement of ITO/MgF_2 cell over ITO cell is 0.55 mA/cm^2, which is lower than the 0.75 mA/cm^2 in IWO case. This is related to the non-ideal DLARC use [54]. Optimization on the DLARC design and corresponding experimental validation are out of the scope of this work, thus will not be further elucidated.

Furthermore, according to Ding *et al.* [6] and Lerat *et al.* [24], significantly improved blue response in IWO cell accounts for the J_{SC} increase with respect to ITO cell while no NIR contribution was observed. This is different from our observations that improved NIR response contributes to the J_{SC_EQE} increase of the as-fabricated IWO cell over ITO cell. Considering that the reference ITO film used by Lerat *et al.* was in a similar N_e range as the one we use in our work, we speculate the rationale of the different optical response in IWO cells may lie in the microstructure and carrier conductive mechanism difference in the IWO films [7,52]. To better interpret the improved optical property of our moderate mobility IWO layer, elaborated investigation based on density functional theory is under investigation.

4. Conclusions

We optimized RF magnetron sputtered IWO TCO at room temperature by adjusting the O_2-to-Ar gas flow ratio during deposition process. The opto-electrical properties of the TCO layers were found to be sensitive to the substrate materials and post-annealing process. The opto-electrical properties of the IWO were manipulated when deposited on top of thin-film silicon layers. This needs to be considered in practical simulation and experimental work. The optimal IWO on glass shows carrier density and mobility of 2.1 × 10^{20} cm^{-3} and 34 cm^2 V^{-1}s^{-1}, which were tuned to 2.0 × 10^{20} cm^{-3} and 47 cm^2 V^{-1}s^{-1}, as well as 1.9 × 10^{20} cm^{-3} and 42 cm^2 V^{-1}s^{-1}, after treated on *i/n*/glass and *i/p*/glass substrates, respectively. Further, GenPro4 simulations implied a clearly increased visible-to-near-infrared optical response in IWO-based SHJ cell with respect to the ITO-based cell, which was demonstrated in practical comparative SHJ devices. Applying MgF_2 as double-layer antireflection coating on top of the optimal device, the EQE-integrated short circuit current density was improved from 39.41 mA/cm^2 to 40.16 mA/cm^2. Our final 8.97-cm^2 wide IWO/MgF_2-based solar cell showed an active area cell efficiency of 22.92%, which is an absolute 0.98% efficiency gain compared to the ITO counterpart, mainly due to its current gain of 1.48 mA/cm^2.

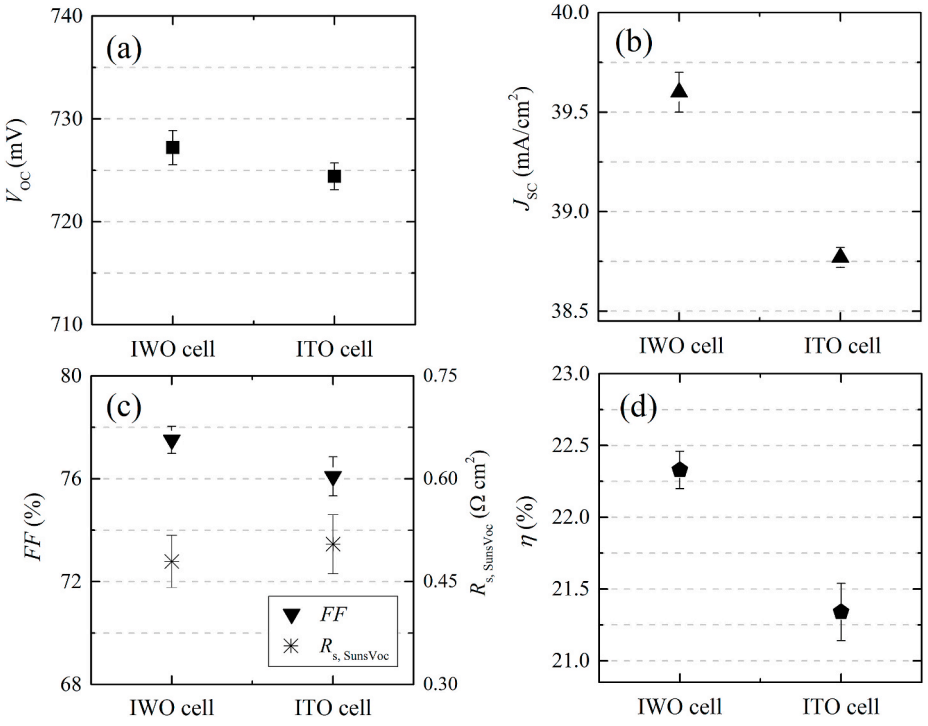

Fig. 7. (a) Open-circuit voltage, V_{OC}, (b) short-circuit current density, J_{SC}, (c) fill factor, *FF*, and series resistance, $R_{s,\ SunsVoc}$, and (d) illuminated area power conversion efficiency, η of the IWO- and ITO-based SHJ devices. The cell area is 8.97 cm^2 and the metal coverage is 1.93%. The results are based on five batches of cells.

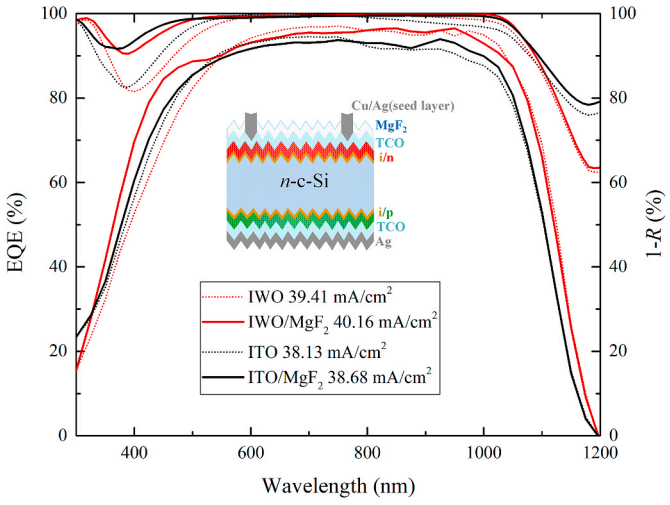

Fig. 8. EQE and 1-*R* of the optimal IWO-based SHJ device and its ITO counterpart, with and without MgF_2 top layer. Inset is the final device structure.

Table 1
Solar cell parameters of the optimal IWO-based SHJ device and its ITO counterpart, before and after MgF_2 top layer deposition (cell area 8.97 cm^2).

	V_{OC} (mV)	J_{SC_EQE}, (mA/cm^2)	*FF* (%)	$\eta_{act.}$ (%)
IWO	730	39.41	78.27	22.52
IWO/MgF_2	731	40.16	78.07	22.92
ITO	728	38.13	78.00	21.65
ITO/MgF_2	728	38.68	77.91	21.94

Declaration of competing interest

The authors declare that they have no known competing financial interests or personal relationships that could have appeared to influence the work reported in this paper.

Acknowledgements

The work has been supported by the Science and Technology Program of Guangdong Province (no. 2019B090918006). C. Han and X. Zhang acknowledge the Overseas Expertise Introduction Project for Discipline Innovation of Higher Education of China (Grant No. B16027), Tianjin Science and Technology Project (Grant No. 18ZXJMTG00220), and Key R&D Program of Hebei Province (No. 19214301D). The authors thank Martijn Tijssen, Daragh O'Connor, Stefaan Heirman, Remko Koornneef from PVMD group for their technical support, Dr. Gianluca Limodio and Dr. Nasim Rezaei in PVMD group as well as Dr. ir. Johannes van Wingerden in Else Kooi Lab for their support with Cu-plating basic flowchart, ellipsometry fitting for stacked layers, and SEM measurements, respectively.

Appendix A. Supplementary data

Supplementary data to this article can be found online at https://doi.org/10.1016/j.solmat.2021.111082.

Credit author statement

Can Han: Conceptualization, Methodology, Investigation, Validation, Formal analysis, Visualization, Writing - original draft. Yifeng Zhao: Resources, Writing - Original draft preparation. Luana Mazzarella: Conceptualization, Writing - Reviewing and Editing, Supervision. Rudi Santbergen: Software, Validation, Writing - Reviewing and Editing. Ana Montes: Resources, Writing - Reviewing and Editing. Paul Procel: Writing - Reviewing and Editing. Guangtao Yang: Writing- Reviewing

and Editing. Xiaodan Zhang: Writing- Reviewing and Editing. Miro Zeman: Supervision, Project administration, Funding acquisition. Olindo Isabella: Supervision, Writing - Reviewing and Editing.

References

[1] A. Descoeudres, Z.C. Holman, L. Barraud, S. Morel, S. De Wolf, C. Ballif, 21% Efficient silicon heterojunction solar cells on n- and p-type wafers compared, IEEE J. Photovolt. 3 (2013) 83–89.

[2] A. Cruz, E.-C. Wang, A.B. Morales-Vilches, D. Meza, S. Neubert, B. Szyszka, R. Schlatmann, B. Stannowski, Effect of front TCO on the performance of rear-junction silicon heterojunction solar cells: insights from simulations and experiments, Sol. Energy Mater. Sol. Cell. 195 (2019) 339–345.

[3] Z.C. Holman, M. Filipič, A. Descoeudres, S. De Wolf, F. Smole, M. Topič, C. Ballif, Infrared light management in high-efficiency silicon heterojunction and rear-passivated solar cells, J. Appl. Phys. 113 (2013), 013107.

[4] S. De Wolf, A. Descoeudres, Z.C. Holman, C. Ballif, High-efficiency silicon heterojunction solar cells: a review, Green 2 (2012) 7–24.

[5] M. Boccard, L. Antognini, V. Paratte, J. Haschke, M. Truong, J. Cattin, J. Dréon, W. Lin, L.L. Senaud, B. Paviet-Salomon, S. Nicolay, M. Despeisse, C. Ballif, Hole-selective front contact stack enabling 24.1%-efficient silicon heterojunction solar cells, IEEE J. Photovolt. (2020) 1–7.

[6] L. Ding, J. Diaz, G. Christmann, L.L. Senaud, L. Barraud, A. Descoeudres, N. Badel, M. Despeisse, S. Nicolay, C. Ballif, High Mobility IWO for Improved Current in Heterojunction Technology Solar Cells, PVSEC 35th EU PVSEC, 2018, pp. 1–15.

[7] S. Calnan, A.N. Tiwari, High mobility transparent conducting oxides for thin film solar cells, Thin Solid Films 518 (2010) 1839–1849.

[8] T. Koida, Y. Ueno, H. Shibata, In2O3-Based transparent conducting oxide films with high electron mobility fabricated at low process temperatures, Phys. Status Solidi (a) 215 (2018) 1700506.

[9] Y. Smirnov, L. Schmengler, R. Kuik, P.-A. Repecaud, M. Najafi, D. Zhang, M. Theelen, E. Aydin, S. Veenstra, S. De Wolf, M. Morales-Masis, Scalable pulsed laser deposition of transparent rear electrode for perovskite solar cells, Adv. Mater. Technol. 6 (2021) 2000856.

[10] Z. Yao, W. Duan, P. Steuter, J. Hüpkes, A. Lambertz, K. Bittkau, M. Pomaska, D. Qiu, K. Qiu, Z. Wu, H. Shen, U. Rau, K. Ding, Influence of oxygen on sputtered titanium-doped indium oxide thin films and their application in silicon heterojunction solar cells, Solar RRL 5 (2020) 2000501.

[11] J.E.N. Swallow, B.A.D. Williamson, S. Sathasivam, M. Birkett, T.J. Featherstone, P. A.E. Murgatroyd, H.J. Edwards, Z.W. Lebens-Higgins, D.A. Duncan, M. Farnworth, P. Warren, N. Peng, T.-L. Lee, L.F.J. Piper, A. Regoutz, C.J. Carmalt, I.P. Parkin, V. R. Dhanak, D.O. Scanlon, T.D. Veal, Resonant doping for high mobility transparent conductors: the case of Mo-doped In2O3, Mater. Horizons 7 (2020) 236–243.

[12] E. Kobayashi, Y. Watabe, T. Yamamoto, Y. Yamada, Cerium oxide and hydrogen co-doped indium oxide films for high-efficiency silicon heterojunction solar cells, Sol. Energy Mater. Sol. Cell. 149 (2016) 75–80.

[13] G.H. Wang, C.Y. Shi, L. Zhao, H.W. Diao, W.J. Wang, Transparent conductive Hf-doped In2O3 thin films by RF sputtering technique at low temperature annealing, Appl. Surf. Sci. 399 (2017) 716–720.

[14] J.G. Kim, J.E. Lee, S.M. Jo, B.D. Chin, J.Y. Baek, K.J. Ahn, S.J. Kang, H.K. Kim, Room temperature processed high mobility W-doped In2O3 electrodes coated via in-line arc plasma ion plating for flexible OLEDs and quantum dots LEDs, Sci. Rep. 8 (2018) 12019.

[15] J. Yu, J. Bian, W. Duan, Y. Liu, J. Shi, F. Meng, Z. Liu, Tungsten doped indium oxide film: ready for bifacial copper metallization of silicon heterojunction solar cell, Sol. Energy Mater. Sol. Cell. 144 (2016) 359–363.

[16] J. Yu, J. Zhou, J. Bian, L. Zhang, Y. Liu, J. Shi, F. Meng, J. Liu, Z. Liu, Improved opto-electronic properties of silicon heterojunction solar cells with SiO x/ Tungsten-doped indium oxide double anti-reflective coatings, Jpn. J. Appl. Phys. 56 (2017), 08MB09.

[17] Y. Zhang, Electronegativities of elements in valence states and their applications. 2. A scale for strengths of Lewis acids, Inorg. Chem. 21 (1982) 3889–3893.

[18] M. Yang, J. Feng, G. Li, Q. Zhang, Tungsten-doped In2O3 transparent conductive films with high transmittance in near-infrared region, J. Cryst. Growth 310 (2008) 3474–3477.

[19] Z. Lu, F. Meng, Y. Cui, J. Shi, Z. Feng, Z. Liu, High quality of IWO films prepared at room temperature by reactive plasma deposition for photovoltaic devices, J. Phys. Appl. Phys. 46 (2013), 075103.

[20] D. Menzel, M. Mews, B. Rech, L. Korte, Electronic structure of indium-tungsten-oxide alloys and their energy band alignment at the heterojunction to crystalline silicon, Appl. Phys. Lett. 112 (2018), 011602.

[21] Y. Zhao, P. Procel, C. Han, L. Mazzarella, G. Yang, A. Weeber, M. Zeman, O. Isabella, Design and optimization of hole collectors based on nc-SiOx:H for high-efficiency silicon heterojunction solar cells, Sol. Energy Mater. Sol. Cell. 219 (2021) 110779.

[22] F. Meng, J. Shi, Z. Liu, Y. Cui, Z. Lu, Z. Feng, High mobility transparent conductive W-doped In2O3 thin films prepared at low substrate temperature and its application to solar cells, Sol. Energy Mater. Sol. Cell. 122 (2014) 70–74.

[23] T. Koida, J. Nishinaga, Y. Ueno, H. Higuchi, H. Takahashi, M. Iioka, Y. Kamikawa, H. Shibata, S. Niki, Improved efficiency of Cu(In,Ga)Se2 mini-module via high-mobility In2O3:W,H transparent conducting oxide layer, Prog. Photovoltaics Res. Appl. 27 (2019) 491–500.

[24] J.F. Lerat, G. Christmann, L. Ding, M. Tomassini, J.J. Diaz Leon, V. Barth, S. Nicolay, D. Munoz, Bringing Tungsten-Doped Indium Oxide to Manufacturing Maturity for High Efficiency Silicon Heterojunction Solar Cells, EUPVSEC, 2019, pp. 1–16.

[25] G. Limodio, Y.D. Groot, G.V. Kuler, L. Mazzarella, Y. Zhao, P. Procel, G. Yang, O. Isabella, M. Zeman, Copper-plating metallization with alternative seed layers for c-Si solar cells embedding carrier-selective passivating contacts, IEEE J. Photovolt. 10 (2020) 372–382.

[26] C. Han, G. Yang, A. Montes, P. Procel, L. Mazzarella, Y. Zhao, S. Eijt, H. Schut, X. Zhang, M. Zeman, Realizing the potential of RF-sputtered hydrogenated fluorine-doped indium oxide as an electrode material for ultrathin SiO x/poly-Si passivating contacts, ACS Appl. Energy Mater. 3 (2020) 8606–8618.

[27] R. Santbergen, T. Meguro, T. Suezaki, G. Koizumi, K. Yamamoto, M. Zeman, GenPro4 optical model for solar cell simulation and its application to multijunction solar cells, IEEE J. Photovolt. 7 (2017) 919–926.

[28] L.T. Yan, R.E.I. Schropp, Changes in the structural and electrical properties of vacuum post-annealed tungsten- and titanium-doped indium oxide films deposited by radio frequency magnetron sputtering, Thin Solid Films 520 (2012) 2096–2101.

[29] J.H. Kim, Y.-H. Shin, T.-Y. Seong, S.-I. Na, H.-K. Kim, Rapid thermal annealed WO3-doped In2O3films for transparent electrodes in organic photovoltaics, J. Phys. Appl. Phys. 45 (2012) 395104.

[30] D.M. Mattox, Fundamentals of ion plating, J. Vac. Sci. Technol. 10 (1973) 47–52.

[31] E. Burstein, Anomalous optical absorption limit in InSb, Phys. Rev. 93 (1954) 632–633.

[32] R.R. Krishnan, V. Kavitha, S. Chalana, R. Prabhu, V.M. Pillai, Effect of tungsten doping on the properties of in 2 O 3 films, JOM 71 (2019) 1885–1896.

[33] P. Reunchan, X. Zhou, S. Limpijumnong, A. Janotti, C.G. Van de Walle, Vacancy defects in indium oxide: an ab-initio study, Curr. Appl. Phys. 11 (2011) S296–S300.

[34] J.Y.W. Seto, The electrical properties of polycrystalline silicon films, J. Appl. Phys. 46 (1975) 5247–5254.

[35] K. Ellmer, A. Klein, B. Rech, Transparent Conductive Zinc Oxide: Basics and Applications in Thin Film Solar Cells, Springer Science & Business Media, 2007, pp. 59–66.

[36] V.H. Nguyen, U. Gottlieb, A. Valla, D. Muñoz, D. Bellet, D. Muñoz-Rojas, Electron tunneling through grain boundaries in transparent conductive oxides and implications for electrical conductivity: the case of ZnO:Al thin films, Mater. Horizons 5 (2018) 715–726.

[37] M. Morales-Masis, S. De Wolf, R. Woods-Robinson, J.W. Ager, C. Ballif, Transparent electrodes for efficient optoelectronics, Adv. Electron. Mater. 3 (2017) 1600529.

[38] H. Fujiwara, M. Kondo, Effects of carrier concentration on the dielectric function of ZnO:Ga andIn2O3:Sn studied by spectroscopic ellipsometry: analysis of free-carrier and band-edge absorption, Phys. Rev. B 71 (2005), 075109.

[39] S. Huang, W. Liu, X. Li, Z. Li, Z. Wu, W. Huang, Y. Yang, K. Jiang, J. Shi, L. Zhang, F. Meng, Z. Liu, Prolonged annealing improves hole transport of silicon heterojunction solar cells, Phys. Status Solidi Rapid Res. Lett. n/a (2021) 2100015.

[40] J. Pan, W. Wang, D. Wu, Q. Fu, D. Ma, Tungsten doped indium oxide thin films deposited at room temperature by radio frequency magnetron sputtering, J. Mater. Sci. Technol. 30 (2014) 644–648.

[41] S. Kumar Vishwanath, T. An, W.-Y. Jin, J.-W. Kang, J. Kim, The optoelectronic properties of tungsten-doped indium oxide thin films prepared by polymer-assisted solution processing for use in organic solar cells, J. Mater. Chem. C 5 (2017) 10295–10301.

[42] A. Cruz, F. Ruske, A. Eljarrat, P.P. Michalowski, A.B. Morales-Vilches, S. Neubert, E. Wang, C.T. Koch, B. Szyszka, R. Schlatmann, B. Stannowski, Influence of silicon layers on the growth of ITO and AZO in silicon heterojunction solar cells, IEEE J. Photovolt. 10 (2020) 703–709.

[43] K.-U. Ritzau, T. Behrendt, D. Palaferri, M. Bivour, M. Hermle, Hydrogen doping of Indium Tin Oxide due to thermal treatment of hetero-junction solar cells, Thin Solid Films 599 (2016) 161–165.

[44] L. Tutsch, H. Sai, T. Matsui, M. Bivour, M. Hermle, T. Koida, The sputter deposition of broadband transparent and highly conductive cerium and hydrogen co-doped indium oxide and its transfer to silicon heterojunction solar cells, Prog. Photovoltaics Res. Appl. (2021) 1–11.

[45] D. Erfurt, T. Koida, M.D. Heinemann, C. Li, T. Bertram, J. Nishinaga, B. Szyszka, H. Shibata, R. Klenk, R. Schlatmann, Impact of rough substrates on hydrogen-doped indium oxides for the application in CIGS devices, Sol. Energy Mater. Sol. Cell. 206 (2020) 110300.

[46] S. Limpijumnong, P. Reunchan, A. Janotti, C.G. Van de Walle, Hydrogen doping in indium oxide: an ab initio study, Phys. Rev. B 80 (2009) 193202.

[47] R. Santbergen, R. Mishima, T. Meguro, M. Hino, H. Uzu, J. Blanker, K. Yamamoto, M. Zeman, Minimizing optical losses in monolithic perovskite/c-Si tandem solar cells with a flat top cell, Opt Express 24 (2016) A1288–A1299.

[48] H. Fujiwara, R.W. Collins, Spectroscopic Ellipsometry for Photovoltaics: Volume 1: Fundamental Principles and Solar Cell Characterization, Springer, 2019, pp. 206–207.

[49] G. Bader, P.V. Ashrit, T. Vo-Van, Transmission and reflection ellipsometry of thin films and multilayer systems, Appl. Opt. 37 (1998) 1146–1151.

[50] P. Procel, H. Xu, A. Saez, C. Ruiz-Tobon, L. Mazzarella, Y. Zhao, C. Han, G. Yang, M. Zeman, O. Isabella, The role of heterointerfaces and subgap energy states on transport mechanisms in silicon heterojunction solar cells, Prog. Photovoltaics Res. Appl. 28 (2020) 935–945.

[51] J.B. Varley, H. Peelaers, A. Janotti, C.G. Van de Walle, Hydrogenated cation vacancies in semiconducting oxides, J. Phys. Condens. Matter 23 (2011) 334212.

[52] K.L. Chopra, S. Major, D.K. Pandya, Transparent conductors—a status review, Thin Solid Films 102 (1983) 1–46.

[53] H. Li, W. Duan, A. Lambertz, J. Hüpkes, K. Ding, U. Rau, O. Astakhov, Influence of room temperature sputtered Al-doped zinc oxide on passivation quality in silicon heterojunction solar cells, IEEE J. Photovolt. 9 (2019) 1485–1491.
[54] D. Zhang, I.A. Digdaya, R. Santbergen, R.A.C.M.M. van Swaaij, P. Bronsveld, M. Zeman, J.A.M. van Roosmalen, A.W. Weeber, Design and fabrication of a SiOx/ITO double-layer anti-reflective coating for heterojunction silicon solar cells, Sol. Energy Mater. Sol. Cell. 117 (2013) 132–138.
[55] A.B. Morales-Vilches, A. Cruz, S. Pingel, S. Neubert, L. Mazzarella, D. Meza, L. Korte, R. Schlatmann, B. Stannowski, ITO-free silicon heterojunction solar cells with ZnO:Al/SiO2 front electrodes reaching a conversion efficiency of 23%, IEEE J. Photovolt. 9 (2019) 34–39.